Progress in Flight Physics **5** (2013) 169-190
DOI: 10.1051/eucass/201305169

BASE-FLOW SENSITIVITY OF A GENERIC ROCKET FOREBODY TOWARDS SMALL FREESTREAM ANGLES

C. C. Wolf[1], Y. You[2], R. Hörnschemeyer[1], H. Lüdeke[2], and V. Hannemann[2]

[1]Institute of Aeronautics and Astronautics, RWTH Aachen
7 Wüllnerstraße, Aachen 52062, Germany
[2]Institute of Aerodynamics and Flow Technology
German Aerospace Center (DLR)
7 Lilienthalplatz, Braunschweig 38108, Germany
10 Bunsenstraße, Göttingen 37073, Germany

Experimental and numerical investigations have been conducted regarding the wake flow of a generic rocket model in subsonic freestream conditions. The bluff base geometry evokes a recirculation area represented by counterrotating vortices. Experiments using Particle Image Velocimetry (PIV) demonstrate that the spatial organization of this area is heavily dependent on small freestream angles ($\alpha, \beta < 1°$), associated with a significant shift in the base pressure distribution. Numerical studies using Reynolds-Averaged Navier–Stokes (RANS) methods with one- and two-equation turbulence models are able to predict the mean velocity field as well as tendencies regarding α and β, but lack the sensitivity of the experiments. The mean pressure level on the base is calculated within 10% of the experimental value using the two-equation turbulence model, although the pressure distributions on the base show distinct differences.

NOMENCLATURE

$c_{p,\mathrm{base}}$	Base pressure coefficient
D	Diameter
DEHS	Di-Ethyl-Hexyl-Sebacat
k, TKE	Turbulent kinetic energy
L	Model length
Ma_∞	Freestream Mach number
N	Total number of samples

Nd:YAG	Neodymium-doped yttrium aluminum garnet
P_k	Production term of k
PIV	Particle Image Velocimetry
RANS	Reynolds-Averaged Navier–Stokes
r	Radial coordinate
Re	Reynolds number
SA	Spalart–Allmaras
SST	Shear stress transport
T_U	Turbulence level
U_∞	Freestream velocity
u, v, w	Velocity components along x, y, z directions
u', v', w'	Fluctuation velocities along x, y, z directions
$\hat{u}, \hat{v}, \hat{w}$	Turbulence intensities along x, y, z directions
x, y, z	Cartesian coordinates
y^+	Nondimensional wall distance
α	Angle of attack
β	Yaw angle
ν_k	Turbulent kinematic viscosity

1 INTRODUCTION

Numerous studies concentrate on the base flow of bluff bodies. Regarding technically relevant Reynolds numbers, the wake is dominated by unsteady effects such as Kármán vortex shedding, Kelvin–Helmholtz structures, and small-scale turbulence. Even though the instantaneous velocity distributions are inherently nonsymmetric, the time-averaged flow field reveals a symmetric pattern dominated by counterrotating vortices forming a recirculation area. In particular, this symmetric layout is observed for (quasi)-two-dimensional (2D) cylinders placed perpendicular to the freestream direction (see, e. g., [1]), since this geometry is ambiguous towards the incidence angle of attack. In contrast, van Oudheusden *et al.* [2] investigate a 2D body with square cross section, revealing distinct changes in the structure of the wake for different angles of attack in the range of 0° to 15°.

The wake of three-dimensional (3D), cylindrical geometries placed in freestream direction can be interpreted as a rotationally symmetric, toroidal extension of 2D test cases. In particular, this can be demonstrated in absence of asymmetries induced by the model support, as shown by Porteiro and Perez-Villar [3] using an upstream sting mounted in the wind tunnel nozzle, or Higuchi *et al.* [4] using a magnetic model suspension system. In the latter case, a total of 2000 instantaneous flowfields captured by PIV were averaged to estab-

lish the ring-like structure of the recirculation area. Nevertheless, some studies suggest that the 3D base flow exhibits a pronounced sensitivity towards small disturbances, such as those in the inflow conditions. Mitchell *et al.* [5] conduct investigations for $\mathrm{Re}_D \approx 9 \cdot 10^5$ ($U_\infty = 50$ m/s) using a model geometry comparable to the present case. The spatial distribution of base pressure as well as the base drag coefficient $c_{p,\mathrm{base}}$ reveal a strong dependency upon freestream angles. While the angle of attack was varied between 0° and 8°, it was also found that a small misalignment of the yaw angle as low as 0.3° notably affected the results.

In this paper, the flow behind the base of a generic rocket is studied experimentally and numerically. The main concerns are addressed to the time-averaged flowfield and turbulence levels. Section 2 introduces the geometry and flow conditions in the test section, as well as the PIV setup and the RANS turbulence model settings. Section 3 describes and compares the flow features observed in the experiment and predicted by simulations. As a starting point, subsection 3.1 deals with studies conducted without angle of attack ($\alpha = 0°$) and without yaw angle ($\beta = 0°$). In the following subsections, investigations regarding flow sensitivity towards the yaw angle and the angle of attack are discussed. The last subsection 3.4 discusses the base pressure distribution. Generally, the focus of this paper is on the main flow patterns of the subsonic bluff-body base flow and the applicability of the RANS turbulence models to predict the flow structures and sensitivities.

2 MODEL GEOMETRY AND SETUP

The generic rocket geometry consists of a slender cylindrical main body (D = 108 mm) with an adjoined conical nose section, supported by a NACA-profiled sting mount. The overall length-to-diameter ratio equals to 10. Additional geometrical details can be taken from Fig. 1. The size of the sting support is large in comparison to other wake investigations, posing a nonnegligible influence on the base flow. However, this is accepted as future measurements will incorporate a thrust nozzle simulation, which requires an adequate pressurized air supply to the model. The investigations are conducted in the open test section (diameter 1500 mm) of a closed-circuit wind tunnel for subsonic

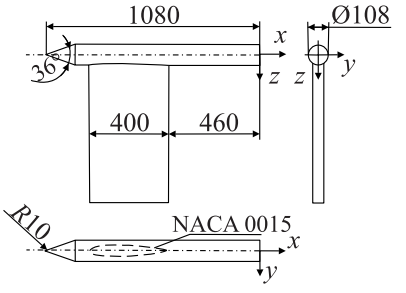

Figure 1 Model geometry — side, front and top view. Dimensions are in millimeters

freestream conditions ($\mathrm{Ma}_\infty = 0.2$) and Reynolds number of $\mathrm{Re}_L = 4.5 \cdot 10^6$ based on the total length of the model.

2.1 Experimental Methodology

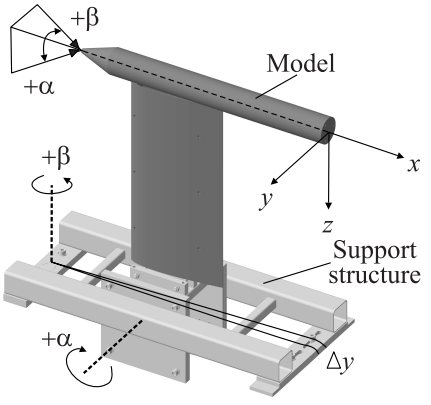

Figure 2 Three-dimensional view of the support structure

The model is mounted on a support structure, allowing adjustment of the angles of attack and sideslip via pivot joints. Precise values for the angular settings are obtained by measuring the corresponding off-axis translational displacement at a distance of 650 mm (α) and 1,150 mm (β) with respect to the axis of rotation. The maximum (random) reading errors are estimated to $\Delta\alpha = 0.045°$ and $\Delta\beta = 0.025°$, respectively. The operating principle of the support structure is outlined in Fig. 2.

The spatial distribution of the base pressure coefficient is determined using 63 pressure taps, allocated uniformly between $r/D = 0$ and 0.42 (positions are shown in Fig. 15*a*). All pressure taps are connected through a switching device to static differential pressure transducers, measuring the difference between base and ambient pressure. The nonlinearity error of the transducers is negligible ($\Delta c_p < 10^{-3}$) for the considered range. The integration time is set to 30 s in order to improve the 95 percent confidence level of the mean value, yielding a similar small error level ($\Delta c_p < 1.5 \cdot 10^{-3}$). Signal drift is compensated by regular zero-offset measurements.

Snapshots of the instantaneous wake flow are determined using a PIV system. A double-pulsed, frequency-doubled Nd:YAG-laser (pulse energy 120 mJ) and a cylinder lens are used to generate a light sheet of about 5 mm in thickness, illuminating vaporized Di-Ethyl-Hexyl-Sebacat (DEHS) oil droplets serving as tracer particles in the airflow. The scene is captured using a calibrated 4 MPix double shutter camera. Particle shifts between two successive light pulses are calculated using an adaptive cross-correlation algorithm. The size of the final interrogation window is set to $(64 \text{ pixel})^2$, in combination with an overlap of 75% resulting in a vector spacing between 1.3 and 1.6 mm, depending on the measurement plane. The PIV setup for the vertical (x, z)-plane is depicted in Fig. 3. Statistical information on the flowfield are derived using $N = 465$ instantaneous snapshots. While the average value of the velocities converged rapidly, the cor-

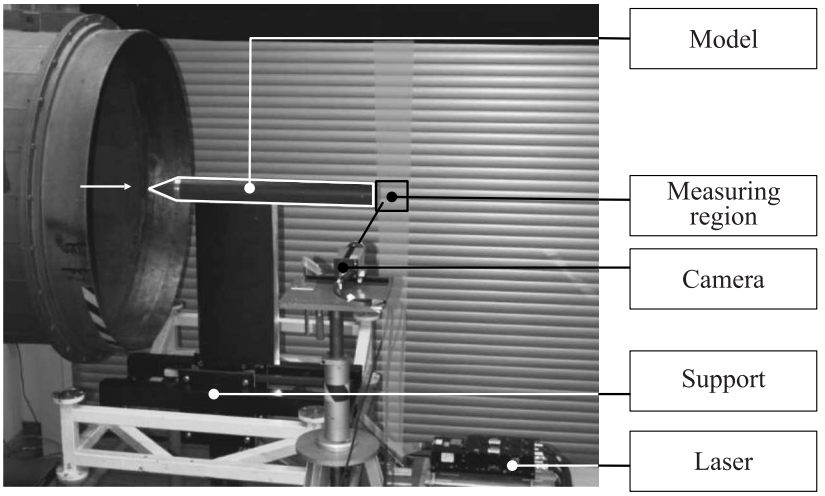

Figure 3 The PIV wind tunnel setup

responding distribution of the standard deviation was not completely smooth for the given number of samples. Nevertheless, a point-wise comparison with hot-wire measurements showed a reasonable agreement [6].

The uncertainty of the PIV measurements was assessed using the methodology presented in [7], which evaluates the main error sources of PIV with respect to different categories that will only be briefly outlined here. Uncertainties induced by the measurement equipment, e. g., calibration or synchronization errors, are very low ($\approx 0.5\%$ of the local velocity). The uncertainty due to a velocity difference between tracer particles and surrounding fluid (slip velocity) was estimated to be below 1.4% of the local velocity level. The results presented in this paper will concentrate on velocity statistics (mean and fluctuation levels). A sampling error lower than 1.9% of the freestream velocity was determined given the finite number of samples N. The most serious source of uncertainty is the PIV correlation algorithm, as it includes a set of highly nonlinear evaluation routines. Velocity distributions obtained in this study were used to generate synthetic particle images as outlined in [7], and reevaluated using the PIV software. A degradation of the data was observed due to random evaluation errors and windowing effects. The impact on the mean velocity levels is below 3% of U_∞. The aforementioned considerations yield a total uncertainty level of around 4% of U_∞.

To determine the $\beta = 0$ condition, the yaw angle is adjusted until the base pressure profile along the y-axis (9 sampling points distributed between $y/D = \pm 0.42$) is symmetric within the error bounds. An adjustment of the neutral

angle of attack cannot be accomplished accordingly, as the pressure distribution is inherently asymmetric towards $z = 0$ due to the influence of the sting wake. Thus, the model is adjusted using a water level device. Regarding the required precision, possible downwash effects of the wind tunnel, and the blockage effect of the sting support, it remains unknown whether this calibration corresponds to the exact aerodynamic zero angle of attack. Nevertheless, conclusions about the sensitivity towards changes in α are still valid.

2.2 Numerical Settings

The DLR TAU code [8] is used to compute the flowfields by solving the RANS equations for compressible flow [9]. The equations are discretited by a second-order finite volume approach on hexahedral grids. Time advancement is carried out by a three-stage Runge–Kutta scheme. The spatial discretitation is based on a central schemes for the investigated subsonic conditions. Two turbulence models, the Spalart–Allmaras (SA) model [10] and the Menter Shear Stress Transport (SST) model [11] are applied to make an assessment of their ability in simulating the subsonic base flows.

Figure 4 displays the computational domain used for base-flow sensitivity study, which is $25D$ in length and $10D$ in diameter. In total, 12 million cells are allocated for this domain. Figure 5 presents a cutaway view through the mesh around the afterbody. In azimuthal direction, the mesh consists of 180 equally spaced points, representing one grid cell every 2°. The near-wall first layer is assigned to be $y^+ \approx 1$ and the boundary layer grid is stretched away from the wall, with a geometrical ratio of 1.15. In addition, the grid close to the trailing edge is clustered towards the base plane in order to resolve the sensitive region.

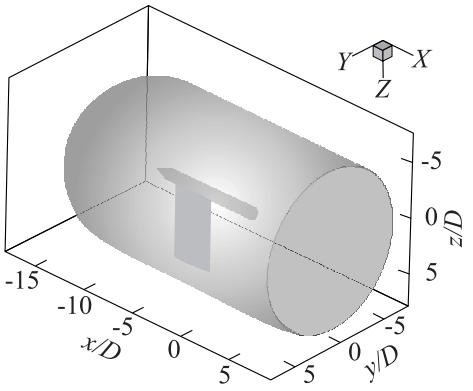

Figure 4 Computational domain of the rocket model

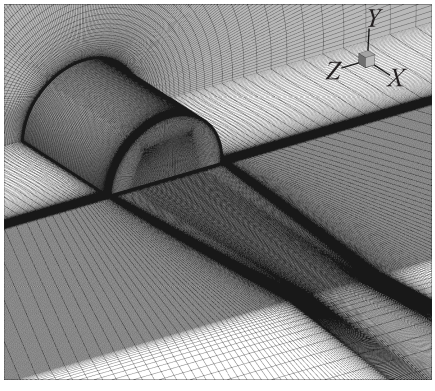

Figure 5 Grid cell distribution around the afterbody

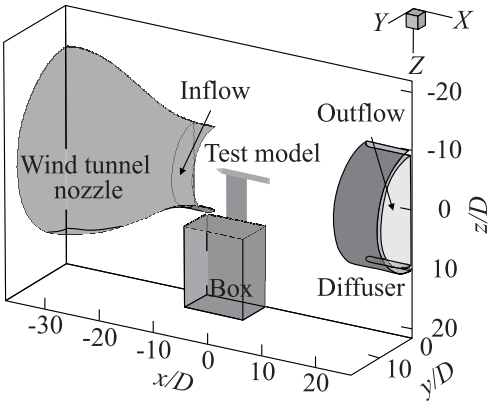

Figure 6 Simplified wind tunnel domain

Some clustered cells, slightly tilted towards the central axis of the cylinder, can also be identified, as free shear layer development is expected there. Further downstream of the base plane ($x/D > 1.5$), the grid density is lowered to control the total amount of grid cells.

The far-field boundary condition was used for the outer surface of the domain. Using far-field boundary condition not far enough from the object of interest could influence the flow solution. An accompanying study [12] of the wind tunnel environment reveals that the core flow shear layer induces a circulation of the surrounding laboratory air.

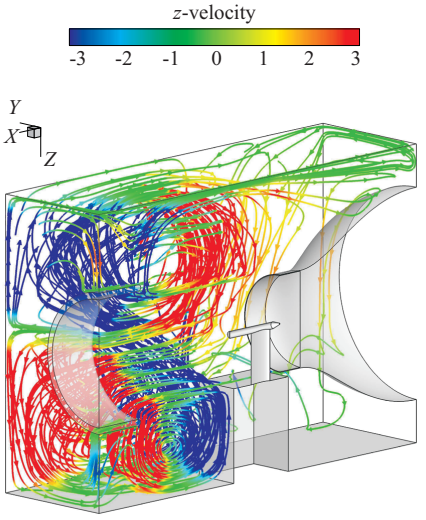

Figure 7 Streamlines colored by the z-velocity.

Figure 6 is the simplified domain of the open test-section wind tunnel. Figure 7 shows that exterior streamlines are driven by the main flow to form a large recirculation. Moreover, a variance of the z-velocity in different parts of the exterior flow are also indicated in the picture. The resulting wind tunnel simulation provides an angle of attack-correction of approximately 0.32° when compared to the nominal 0° far-field boundary condition. Although the near-boundary influence could be responsible

for a part of this correction, the value is smaller than the variation of angles investigated below. Therefore, the angular sensitivity of the experiments might be slightly shifted but still well captured by the numerical simulations, even if the computational domain stays near to the object.

3 RESULTS AND DISCUSSION

3.1 Configuration Without Angle of Attack or Yaw Angle

3.1.1 Mean velocity

Under circumstances of zero angle of attack ($\alpha = 0°$) and zero yaw angle ($\beta = 0°$), both turbulence models (SA and SST) are used to investigate the base flow.

Figure 8 depicts the planar velocity $(u^2+v^2)^{0.5}/U_\infty$ in the (horizontal) (x, y)-plane. The wake flow is governed by a characteristic separation bubble encapsulated between base plane and free shear layers. Within this bubble, a recirculation is evoked by a vortex ring, which in this cross-section view is represented by two counterrotating vortices. Despite careful alignment of the rocket body as outlined in subsection 2.1, the layout of the experimental result (Fig. 8*a*) is only approximately, but not fully symmetric. Both upstream and downstream stagnation points have a minor deviation from the symmetry axis ($y = 0$), and the vortex cores are located at slightly different streamwise positions. In contrast, both numerical results are inherently symmetric and show a similar layout. However, it is obvious that the SA model results in a visibly smaller recirculation region compared with the experimental result. The downstream stagnation point representing the bubble length is located at $x/D = 0.91$, clearly deviating from the experimental result ($x/D = 1.28$). The SST model predicts a reasonable but slightly larger recirculation area, in which the downstream stagnation point remains at $x/D = 1.38$. The streamwise position of the vortex centers also agrees better with the experimental data than the results of the SA model. In Fig. 8*a*, the experimental vortex centers locate at $x/D = 0.70$ and 0.66. The upper center is situated slightly more downstream. The corresponding x-positions of the vortex centers in the SST model (Fig. 8*b*) are $x/D = 0.60$ and 0.59, respectively. The agreement with the experimental data is not perfect but much better than the prediction of $x/D = 0.27$ and 0.28 by the SA model (Fig. 8*c*).

3.1.2 Turbulence level

Due to the better prediction of the mean velocity field, the SST model is chosen for the comparisons with the experimental results in terms of the turbulence level

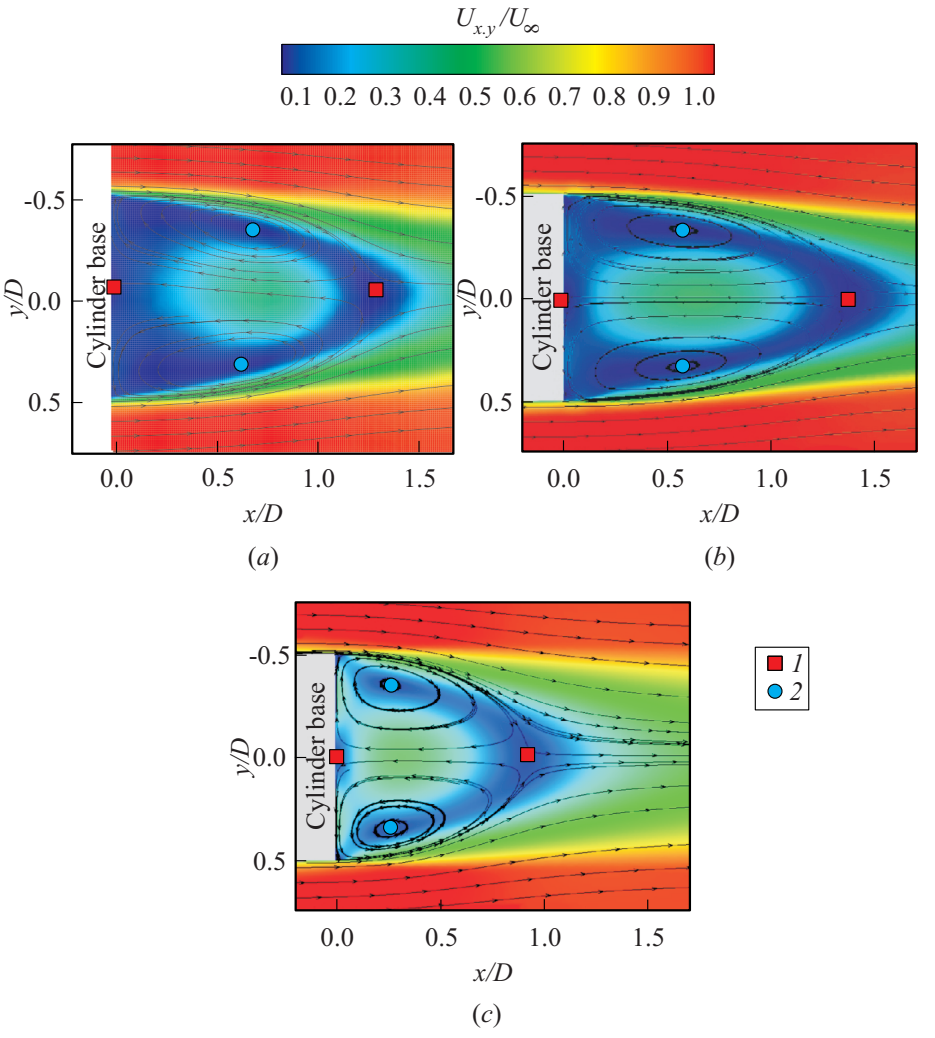

Figure 8 Velocity contours in the (x, y)-plane, $\alpha = 0°$, $\beta = 0°$: (a) experimental result; (b) numerical result, SST model; and (c) numerical result, SA model; *1* — stagnation points; and *2* — vortex centers.

T_u. For bluff-body wake flows, it is well known that the turbulence intensities are anisotropic [1, 13], meaning that

$$\hat{u} = \frac{\sqrt{\overline{u'^2}}}{U_\infty} \neq \hat{v} = \frac{\sqrt{\overline{v'^2}}}{U_\infty} \neq \hat{w} = \frac{\sqrt{\overline{w'^2}}}{U_\infty}$$

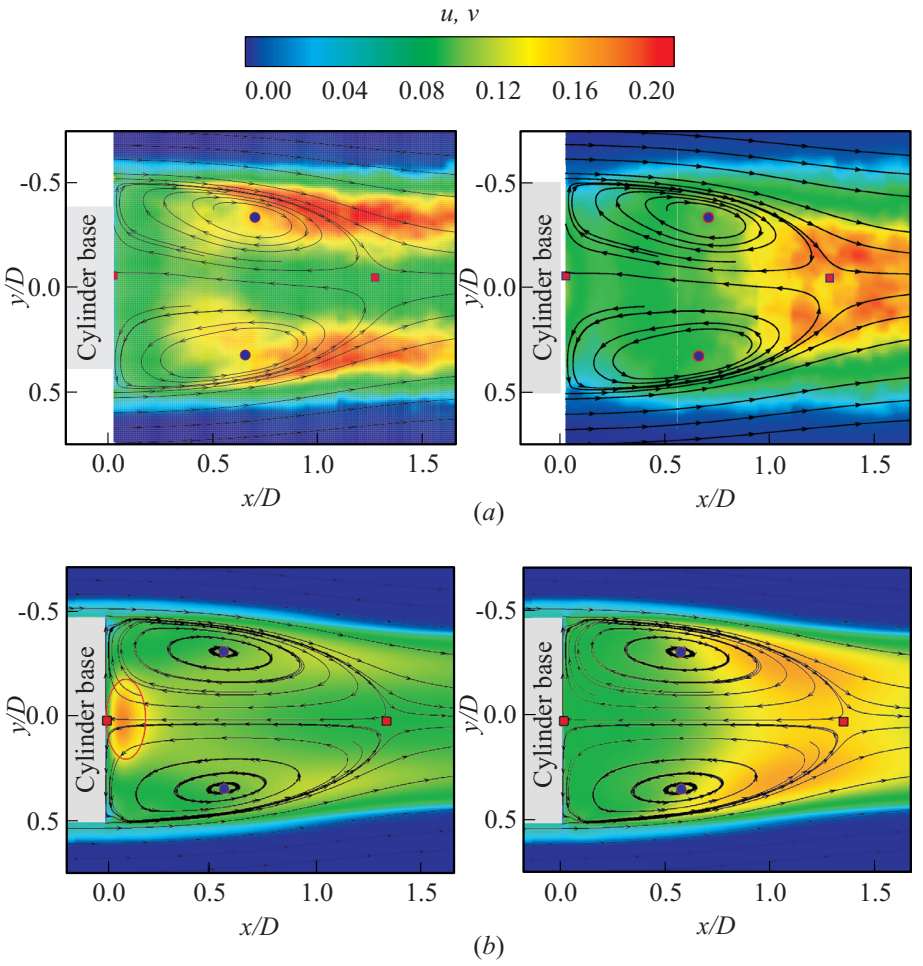

Figure 9 Turbulence levels in the (x, y)-plane, $\alpha = 0°$, $\beta = 0°$: (a) experimental results; and (b) numerical results (SST model). Left column refers to $\hat{u}$ and right column to $\hat{v}$.

for a given location. This was also observed for the current configuration [6]. An example of this behavior is given in Fig. 9. The maximum values of $\hat{v}$ can be found in a region near the rearward stagnation point, centered at the symmetry axis $y = 0$ (Fig. 9a). In contrast, high levels of $\hat{u}$ are located in two disclosed regions at and downstream of the vortex cores (see Fig. 9a).

Although the turbulence model provides only a transport equation for the turbulent kinetic energy, TKE:

$$k = \frac{1}{2}\left(\overline{u'^2} + \overline{v'^2} + \overline{w'^2}\right) .$$

The modeling of the turbulent shear stresses gives different components depending on the velocity gradients of the mean flow. The corresponding numerical $\hat{u}$ and $\hat{v}$ values are depicted in Fig. 9*b*. The numerical turbulent intensities are smaller, but the location of the experimental maxima are reproduced. The SST result identifies another region of relatively high $\hat{u}$ near the base center (encircled red in Fig. 9*b*) which cannot be found in the experimental results. This overprediction of $\hat{u}$ is linked to a misrepresentation of the normal stresses. For the flow near a stagnation point, simplified as a 2D problem, incompressibility yields $\partial u/\partial x = -\partial v/\partial y$. The production term of the TKE, P_k, is formulated as

$$P_k = -\left(\overline{u'^2} - \overline{v'^2}\right)\frac{\partial u}{\partial x} .$$

In reality, $\overline{u'^2} - \overline{v'^2}$ is likely to be small near the wall. The SST model formulation (as well as other linear eddy viscosity models) results in

$$\overline{u'^2} = \frac{2}{3}\,k - 2\nu_t\left(\frac{\partial u}{\partial x}\right) ; \qquad \overline{v'^2} = \frac{2}{3}\,k + 2\nu_t\left(\frac{\partial u}{\partial x}\right) .$$

Consequently,

$$P_k = 4\nu_t\left(\frac{\partial u}{\partial x}\right)^2$$

which leads to excessive generation of P_k. Such an overprediction of TKE is common for stagnation flows, like impinging jets [14]. The transport of turbulent kinetic energy without accounting of the different directions adds to the high amount of predicted turbulence intensity in the stagnation area. More advanced nonlinear eddy viscosity models, e. g., Reynolds stress models, should be considered to improve this aspect of the simulation.

On the one hand, the turbulence intensities are only intermediate terms in the presented turbulence models; on the other hand, the 2D PIV measurements cannot provide all components of the turbulent kinetic energy at the same time. Therefore, the following definition of a 2D turbulence level is used to discuss qualitatively the turbulence level in this paper:

$$T_u = \frac{\sqrt{0.5\left(\overline{u'^2} + \overline{v'^2}\right)}}{U_\infty} .$$

The results for the baseline flowfield ($\alpha, \beta = 0^\circ$) are depicted in Fig. 10. It is observed that the SST model globally reproduces a similar but lower turbulence level compared with the experimental results. In both cases, the regions of high turbulence are located along the shear layers, starting from the vortex centers ($x/D > 0.7$).

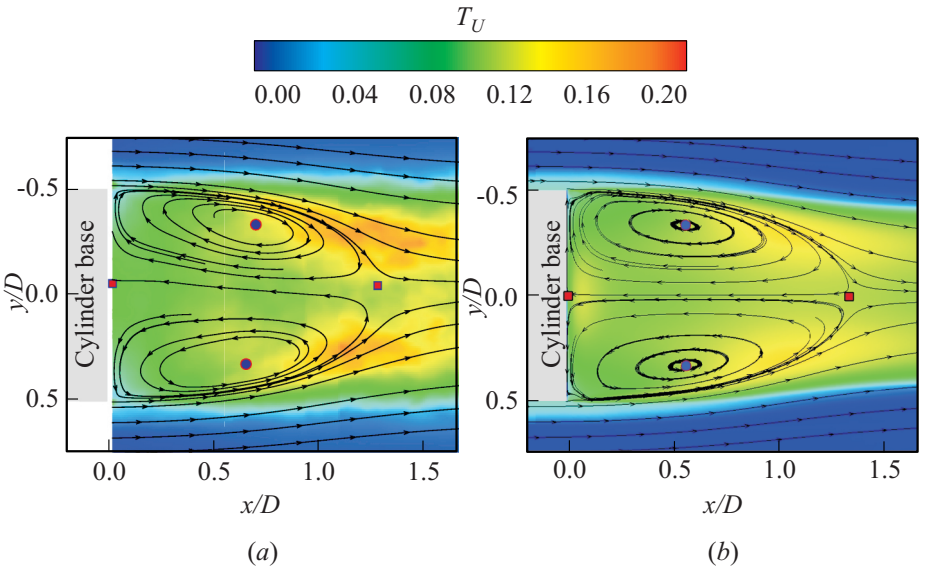

Figure 10 Turbulence levels in the (x, y)-plane, $\alpha = 0°$, $\beta = 0°$: (a) experimental result; and (b) numerical result (SST model).

3.2 Sensitivity Towards Yaw Angle

The experiments reveal that the base flow topology is very sensitive towards small adjustments of the freestream angles well below 1° (see Figs. 11a to 11c for $\beta = -0.3°$, $0.3°$, and $0.75°$). The effects can be summarized as follows. Both stagnation points move from the center line towards the windward side. The size of the lee-sided vortex increases significantly, whereas its center shifts both upstream and towards the center line. In contrast, the windward vortex shrinks and very slightly shifts downstream. The axis of the recirculation flow is accordingly tilted. By examining multiple angles, it can be shown that the effects described above are consistent, meaning that the flow patterns are roughly symmetric regarding $\pm\beta$ (see Figs. 11a and 11b) and become more pronounced with increasing yaw angle (see Figs. 11b and 11c).

Figure 12 presents the corresponding locus curves of stagnation points and vortex centers in the (x, y)-plane for $\beta = -0.75°$–$1.5°$. It is obvious that the flow pattern is most sensitive in the range of $-0.3° \leq \beta \leq 0.3°$, whereas a further increase of the yaw angle beyond $|\beta| > 0.3°$ only has a minor influence. This also explains why the stagnation points for $\beta = 0°$ do not exactly coincidence with the $y = 0$ axis, but exhibit a slight deviation towards a positive value $(y/D = 0.04)$, which matches the level of uncertainty for the symmetric case.

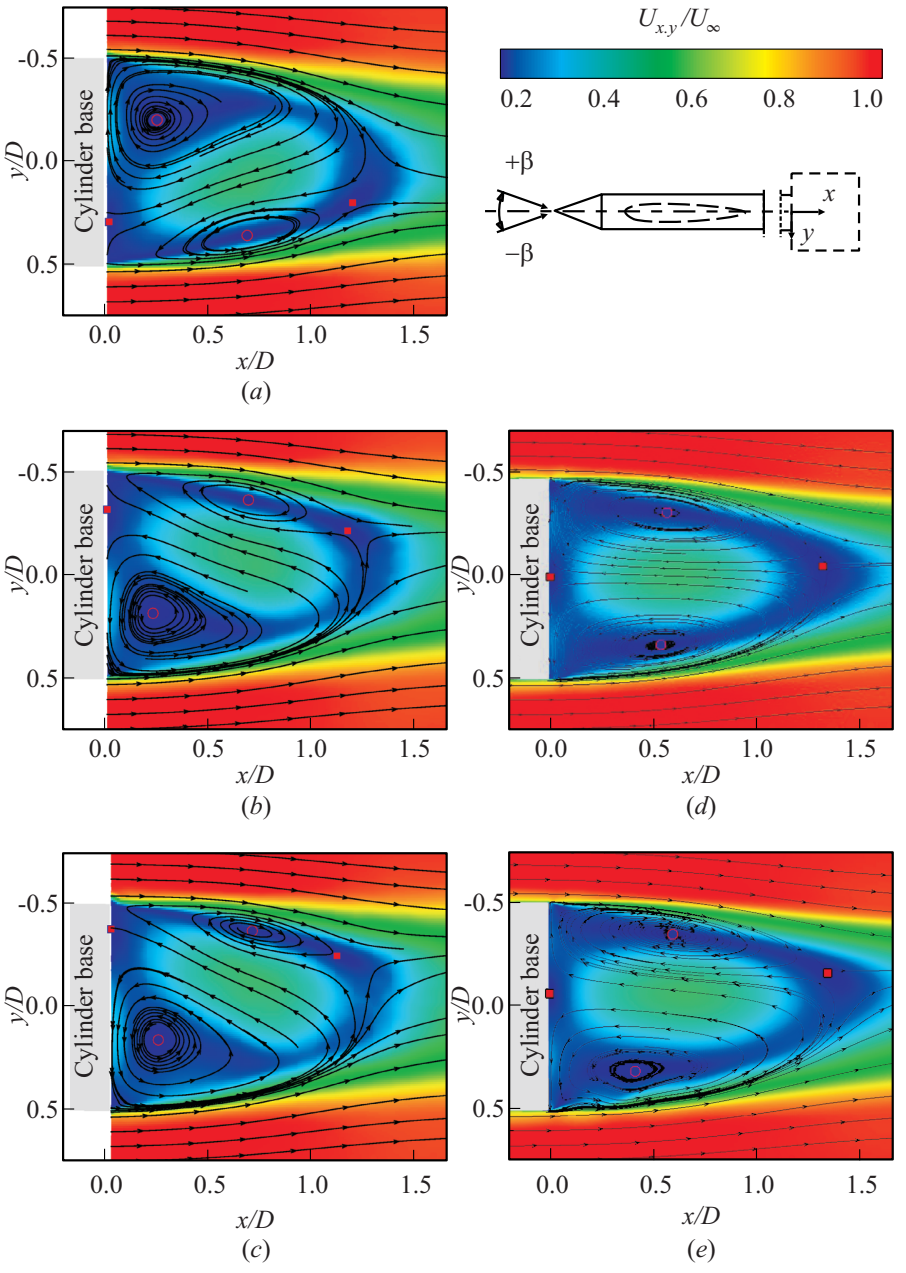

Figure 11 Sensitivity of mean velocity towards yaw angle, $\alpha = 0°$. Experimental results: (*a*) $\beta = -0.3°$; (*b*) 0.3°; and (*c*) $\beta = 0.75°$. The SST model: (*d*) $\beta = 0.35°$; and (*e*) $\beta = 0.7°$.

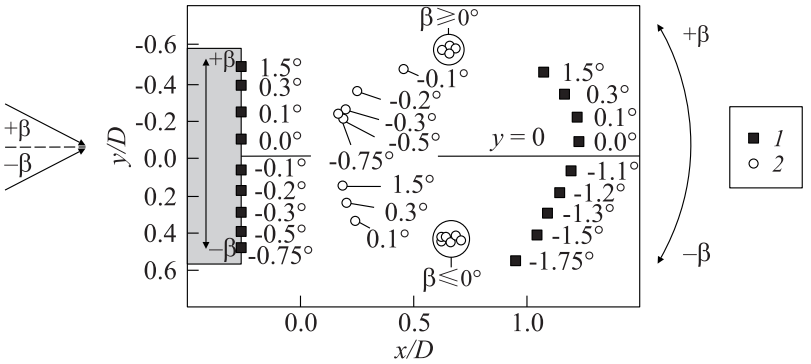

Figure 12 Locus curves of vortex (*1*) cores and stagnation points (*2*) for $\beta = -0.75°$–$1.5°$

Although the SST model exposes some discrepancy to experimental data for $\beta = 0°$, its applicability in studying the sensitivity towards yaw angle (and further on angle-of-attack) is tested (see Figs.11*d* and 11*e*). It was found that the numerical simulations using SST lack the high sensitivity of the experiments. Nevertheless, the flow becomes visibly asymmetric, and the general tendencies (direction of the stagnation point shift and evolution of windward and lee-sided vortex core) match the corresponding experimental data. The distribution of the turbulence levels is also affected by the yaw angles (Fig. 13). The strength of the luff-sided high-turbulence region increases significantly, whereas the lee-sided turbulence level decreases accordingly. Again, the numerical simulation reproduces the correct tendency. Nevertheless, comparing Fig. 13*e* with 13*c*, for example, it is visible that SST model underestimates the high-turbulence region on the windward side.

3.3 Sensitivity Towards Angle of Attack

Similar investigations were conducted regarding the influences of the angle of attack in the (x, z)-plane. For $\alpha = 0°$, the influence of the sting becomes visible in both experimental and numerical results (see Figs. 14*a* and 14*c*). The incoming flow on opposite sides of the cylinder have different velocity profiles. The flow on the lower side has a slower velocity due to the wake of the sting. For example, at x/D=0, z/D=0.7, experimental results reveal a planar velocity of $U_{x,z} = 0.92U_\infty$. The corresponding value taken from the SST simulation is $0.92U_\infty$ as well. Secondly, the wake of the sting affects the symmetry of the recirculation in the position of stagnation points as well as vortex centers.

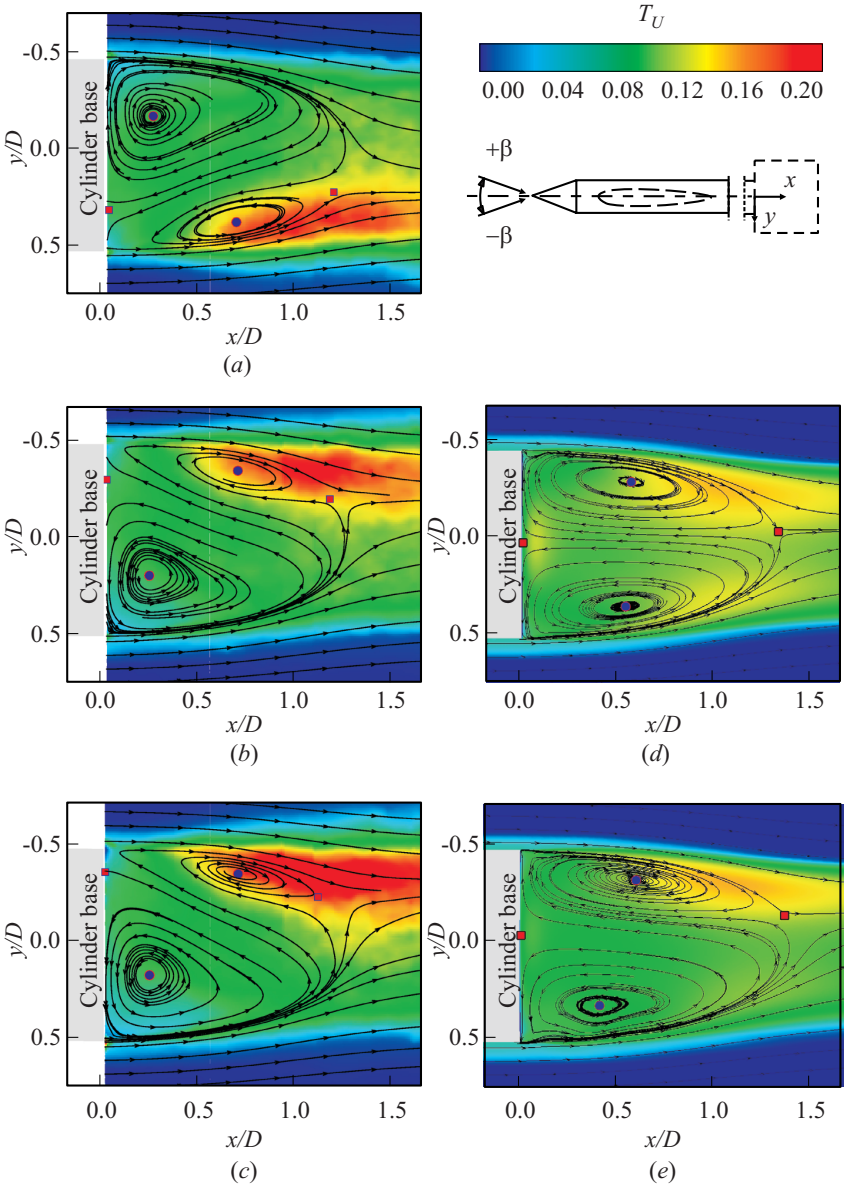

Figure 13 Sensitivity of turbulence levels towards yaw angle, $\alpha = 0°$. Experimental results: (*a*) $\beta = -0.3°$; (*b*) $0.3°$; and (*c*) $\beta = 0.75°$. The SST model: (*d*) $\beta = 0.35°$; and (*e*) $\beta = 0.7°$.

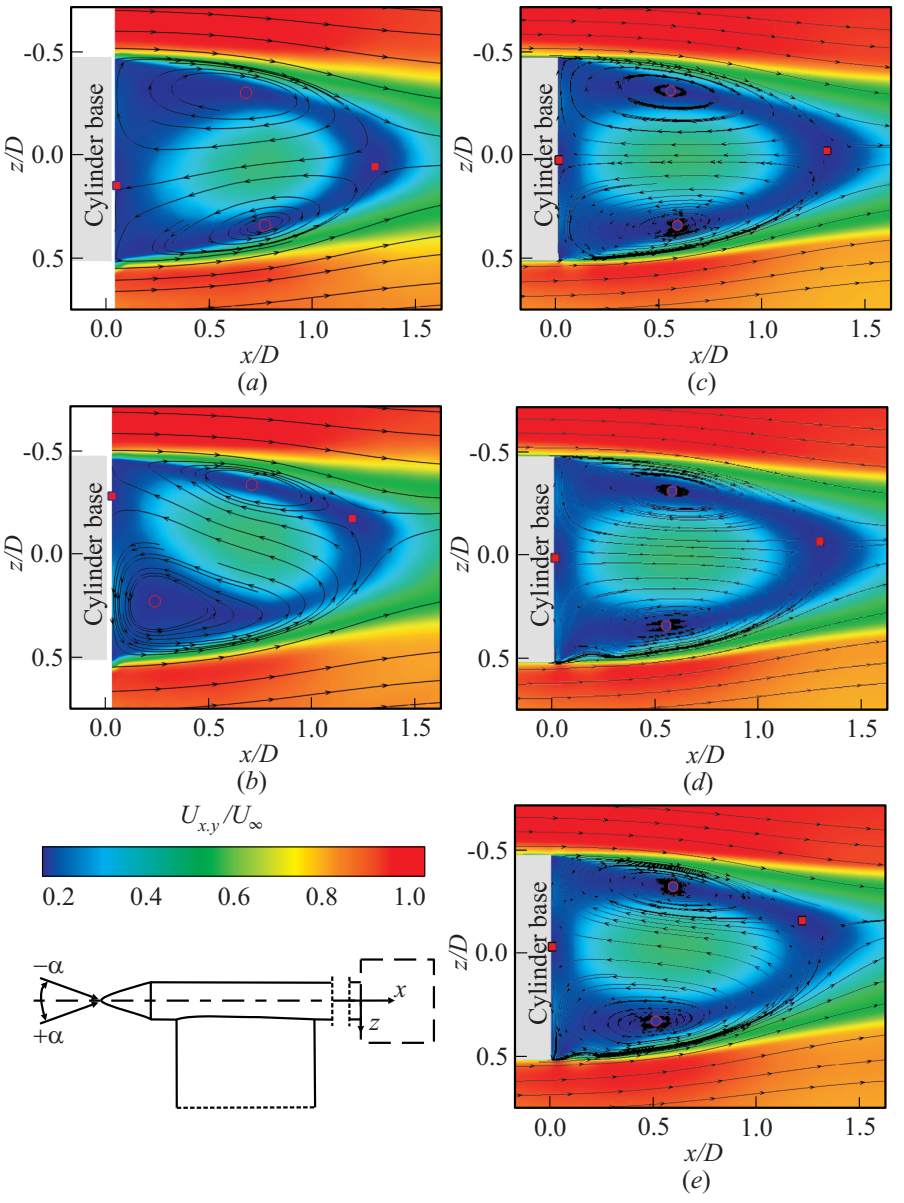

Figure 14 Sensitivity of mean velocity towards angle of attack, $\beta = 0°$. Experimental results: (a) $\alpha = 0°$; and (b) $\alpha = -0.35°$. The SST model: (c) $\alpha = 0°$; (d) $-0.35°$; and (e) $\alpha = -0.97°$.

The angular alignment of the model within the wind tunnel's test section is performed geometrically. Given the expected sensitivity and the blocking effect of the sting, it remains unclear whether this setting corresponds to the aerodynamic $\alpha = 0$. Nevertheless, when comparing Figs.11*b* and 14*b*, it is obvious that the sensitivity towards α is comparable to the β-results, including the corresponding shifts of the flow features. Given the fact that (x, y)- and (x, z)-planes are perpendicular to each other, this implicitly rules out the sting wake as the origin of the described phenomenon. Again, numerical results are able to reproduce the general tendencies of the experimental results, but miss the pronounced sensitivity of the experiments. For example, in the SST-result at $\alpha = -0.97°$ (Fig. 14*e*), the inclination of the recirculation flow is still smaller than in the experimental result at $\alpha = -0.35°$.

3.4 Base Pressure

The base pressure is a key factor in bluff-body aerodynamics, as it describes the interaction between wake flow and body and thus determines the base drag. In this context, van Raemdonck and van Tooren [15] investigated a generic road vehicle for $U_\infty = 60$ m/s. It was shown that the recirculation bubble is tilted in a similar fashion compared with the current investigation, even though the reason is the proximity to the ground board and not the freestream angles. In this case, the asymmetry of the vortex positions is linked to a nonuniform base pressure distribution, which is principally also shown for the generic rocket model.

The averaged $c_{p,\mathrm{base}}$ values are -0.115 for the experimental data, -0.102 for the SST model, and -0.207 for the SA model. In general, this indicates that the SST model again performs better than SA compared with the experimental result.

Figure 15 presents the spatial distribution of the pressure coefficient $c_{p,\mathrm{base}}$ in the model's base plane. It is evident that both numerical results predict a high-pressure region in the center of the base plane (see Figs. 15*b* and 15*c*). The pressure in this region is about 20% higher than the measured pressure. A possible overestimation of the base pressure may be linked to the overprediction of the TKE near the stagnation point, as an artificially increased turbulence level will finally yield an increased static pressure as a result of the momentum equation. The SA model exhibits a ring-like structure of very low pressure ($c_{p,\mathrm{base}} < -0.2$) for $r/D \approx 0.3$, which is assumed to be a consequence of the short recirculation bubble and the proximity of the vortex centers to the base plane.

The experimental $c_{p,\mathrm{base}}$-distribution (see Fig. 15*a*) is expectedly near-symmetric towards $y = 0$. Comparatively low pressure levels can be found in the upper base part ($z < 0$), corresponding to the slightly tilted vortex system observed by PIV measurements (see Fig. 14*a*). The experimental pressure distribution features no clear indication of a stagnation point, which would be

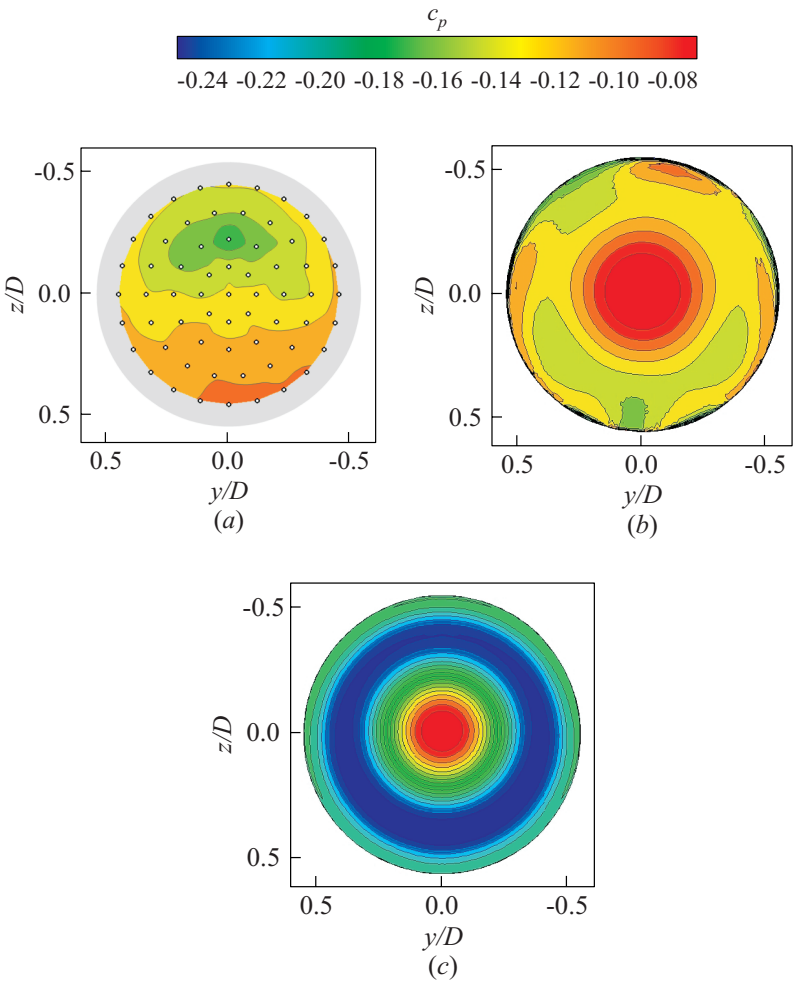

Figure 15 Base pressure levels, $\alpha = 0°$, $\beta = 0°$: (a) experimental result (circles refer to pressure tap); (b) SST model; and (c) SA model.

expected around $y = 0$, $z/D = 0.15$ as seen by PIV results. A possible reason might be an oscillating motion of the stagnation point that diffuses the pressure information over a wider range. However, this cannot be proved as the current measurements do not provide time-resolved measurements.

The pattern of the experimental result can be inverted when decreasing α, as Fig. 16a exemplarily demonstrates for $\alpha = -0.35°$. Since now, the lower vortex slides towards the base plane (compare PIV result in Fig. 14b), the high-pressure region can be found in the upper half (negative z-values). In contrast,

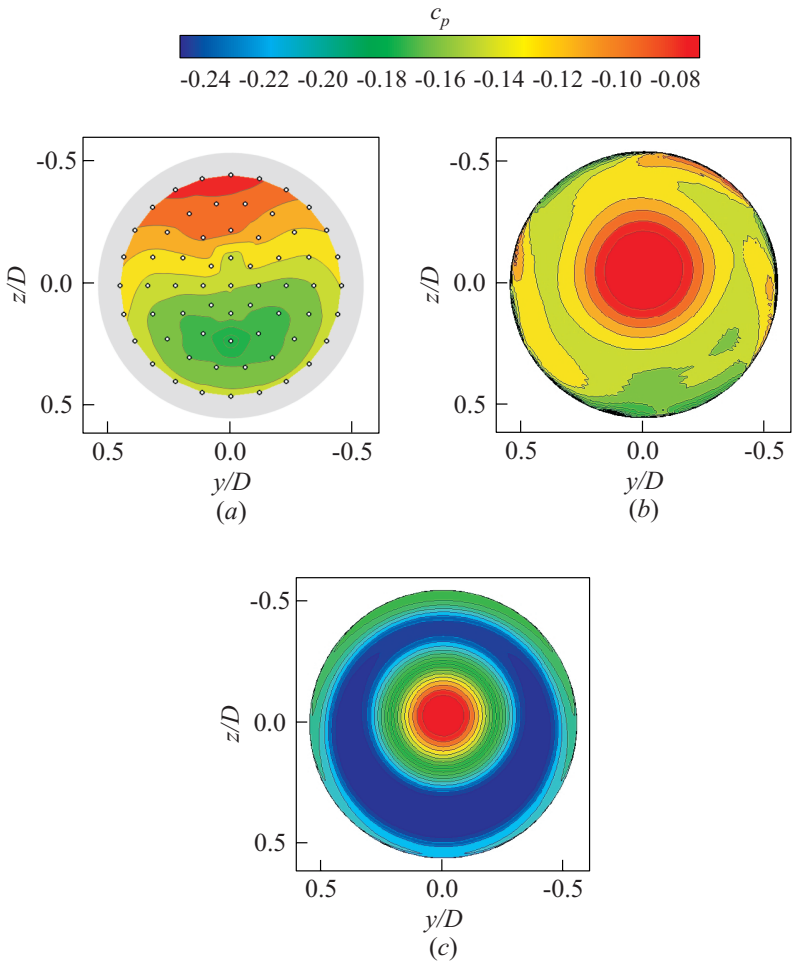

Figure 16 Base pressure levels, $\beta = 0°$: (a) experimental result, $\alpha = -0.35°$; (b) SST model, $\alpha = -0.97°$; and (c) SA model, $\alpha = -0.97°$.

an even larger variation of the angle of attack to $\alpha = -0.97°$ rarely reflects on the pressure distributions as seen by SA or SST models (see Figs. 16b and 16c).

4 CONCLUDING REMARKS AND OUTLOOK

The base flow of a generic rocket model is investigated by experimental and numerical methods. In the case of zero incidence angles, PIV and RANS calcu-

lations using the SST model exhibit comparable results regarding both averaged flowfield and turbulence levels. In contrast, the recirculation bubble simulated by the SA model is predicted too short. The ability to calculate the base pressure levels is limited by an overprediction of the turbulence levels in the stagnation region for both SA and SST models. Despite this problem, the SST model delivers reasonable $c_{p,\mathrm{base}}$ values.

Experimental data show that the wake flow topology of this bluff-based geometry is heavily dependent on small freestream angles. It seems that the symmetric configuration for $\alpha = 0°$, $\beta = 0°$ is unstable and switches to a nonsymmetric pattern for angular deviations (or misalignments) as small as $\pm$ 0.1°. This behavior is shown for both angle of attack and sideslip, indicating that it is not related to the model's sting support. The angular sensitivity is reflected in the positions of stagnation points and vortex cores, the tilt angle of the recirculation, the turbulence levels, and the pressure distribution in the base plane. Corresponding RANS calculations using the Menter SST model are able to capture the same tendencies but lack the distinct sensitivity demonstrated by the experiments. The present work demonstrates the necessity of a careful angular alignment when conducting wind tunnel measurements using blunt shaped models.

Future experimental work will concentrate on the three-dimensionality of the base flow layout. The results discussed in the current work only represent planar slices of a toroidal vortex system. The structure of this system is of great interest in case of the nonsymmetric wake layout (e. g., $\beta \neq 0°$) and is believed to add further insight to the observed phenomena, particularly as the wake of 2D bluff bodies in contrast seems more indifferent towards incidence angles [2].

In the next step, cross-flow (y, z-) measurement planes will be investigated, requiring the application of three-component PIV due to the nonnegligible out-of-plane velocity. Although the current PIV records are not time-resolved, the application of a statistical modal analysis (e. g., Proper Orthogonal Decomposition) will add further information on the unsteadiness of the wake and will be complemented by flush-mounted dynamic pressure transducers. The results are also expected to clarify why the stagnation point at the center of the base is clearly visible in averaged PIV records, but not in averaged experimental base pressure distributions.

Regarding the SST model's shortcoming of overpredicting the TKE level near the stagnation point, a more detailed turbulence model study is planed to be carried out in the future. It will be interesting to check if the suspicious high turbulence level accounts for the error in c_p distribution, and whether further development and validation of RANS models based on this observation is possible. Moreover, a Detached Eddy Simulation (DES) of the present base-flow is on-going [12]. It is also our outlook to study the DES method's ability in capturing such a sensitivity towards small attack/yaw angles.

ACKNOWLEDGMENTS

Financial support has been provided by the German Research Foundation (DFG — Deutsche Forschungsgemeinschaft) in the framework of the Sonderforschungsbereich Transregio 40.

REFERENCES

1. Braza, M., R. Perrin, and Y. Hoarau. 2006. Turbulence properties in the cylinder wake at high Reynolds numbers. *J. Fluids Structures* 22:757–71.
2. Van Oudheusden, B. W., F. Scarano, N. P. van Hinsberg, and D. W. Watt. 2005. Phase-resolved characterisation of vortex shedding in the near wake of a square-section cylinder at incidence. *Exper. Fluids* 39:86–98.
3. Porteiro, J. L. F., and V. Perez-Villar. 1996. Wake development in turbulent subsonic axisymmetric flows. *Exper. Fluids* 21:145–50.
4. Higuchi, H., H. Sawada, and H. Kato. 2006. Separated flow field over blunt circular cylinder suspended magnetically in free-stream direction. AIAA Paper No. 2006-3552.
5. Mitchell, R. R., J. N. Roetzel, F. K. Lu, and J. C. Dutton. 2008. A study of the base pressure distribution of a slender body of square cross-section. AIAA Paper No. 2008-423.
6. Wolf, C. C., R. Henke, and R. Hörnschemeyer. 2010. Investigation on turbulence structures in the wake of a generic rocket configuration. *DGLR STAB-Symposium 2010.* (Also accepted for publication in *Notes on Numerical Fluid Mechanics.*)
7. Lazar, E., B. DeBlauw, N. Glumac, J. C. Dutton, and G. Elliot. 2010. A practical approach to PIV uncertainty analysis. AIAA Paper No. 2010-4355.
8. Schwamborn, D., T. Gerhold, and R. Heinrich. 2006. The DLR TAU-Code: Recent applications in research and industry. *European Conference on Computational Fluid Dynamics, ECCOMAS CFD.*
9. Reimann, B., I. Johnston, and V. Hannemann. 2004. DLR-TAU Code for high enthalpy flows. *Notes Numer. Fluid Mechanics Multidisciplinary Design.* 87:99–106.
10. Spalart, P. R., and S. R. Allmaras. 1992. A one-equation turbulence model for aerodynamic flows. AIAA Paper No. 1992-439.
11. Menter, F. R. 1994. Two-equation eddy-viscosity turbulence models for engineering applications. *AIAA J.* 32:1598–605.
12. You, Y., K. Oßwald, H. Lüdeke, and V. Hannemann. 2011. Detached eddy simulation of the subsonic base flow with a side support. *4th Symposium on Hybrid RANS–LES Methods.*

13. Hu, J. C., and Y. Zhou. 2009. Aerodynamic characteristics of asymmetric bluff bodies. *J. Fluids Engng.* 131:011206-1–011206-9.

14. Craft, T. J., L. J. W. Graham, and B. E. Launder. 1993. Impinging jet studies for turbulence model assessment — II. An examination of the performance of four turbulence models. *Int. J. Heat Mass Transfer* 36:2685–97.

15. Van Raemdonck, G. M. R., and M. J. L. van Tooren. 2008. Time-averaged phenomenological investigation of a wake behind a bluff body. *BBAA 6th Colloquium (International) on Bluff Body Aerodynamics & Applications.*